



CFD 2005

Click on CFDSC Logo to Start

**13th Annual Conference
of the
Computational Fluid Dynamics
Society of Canada**

PROCEEDINGS

TABLE OF CONTENTS

Preface

Keynote Speakers

Unsteady CFD Modeling of Micro-Adaptive Flow Control for an Axisymmetric Body
J. Sahu, K.R. Heavey.....I

Development of a High-Fidelity Numerical Model for Hazard Prediction in the Urban Environment
F.S. Lien, E. Yee, H. Ji, A. Keats, K.J. Hsieh.....IX

Session 1: Hydrodynamics 1

Wakes of Idealized Propeller Shafts With Sleeves
D. Hally1

Numerical Study of Hub Taper Angle on Podded Propeller Performance
M.F. Islam, B. Veitch, N. Bose, P. Liu9

Exploration of Submarine Wake and Powering Performance Using CFD Method
H. Yao, H. Shen, N. Zhang, R. Yang, L. Ying.....16

CFD Study of an Underwater Fin Propulsion System Using a 3D Model
G. Pedro, A. Suleman, N. Djilali24

Numerical Simulation of 3-D Integrated Viscous Flow Field around Axisymmetric Body with Duct
T. Wang, G.W. Yang, G. J. Huang, Y.K. Tian, L.D. Zhou.....32

Session 2: Algorithm 1

A Robust, Efficient and Accurate Beta-pdf Integration Algorithm in Nonpremixed Turbulent Combustion
H. Liu, F.S. Lien, E. Chui.....45

Turbulent Flow over a Square Cylinder with Prescribed and Autonomous Motions
G.P. Thompson and F.S. Lien53

Large Eddy Simulation of High Reynolds Number Channel Flow on Coarse Grids
J. Larsson, F.S. Lien, E. Yee61

Quadtree Space Partitioning for Mapping Two-dimensional Results on Three-dimensional Domains
T. Josey69

Volume-of-Fluid Algorithm on a Non-orthogonal Grid
W. Jang, F.S. Lien, H. Ji76

Development of a High-Fidelity Numerical Model for Hazard Prediction in the Urban Environment

F.S. Lien¹, E. Yee², H. Ji³, A. Keats¹ and K.J. Hsieh¹

¹ *Department of Mechanical Engineering, University of Waterloo, Waterloo, Ontario, N2L 3G1, Canada*

² *Defence R&D Canada - Suffield, P.O. Box 4000, Medicine Hat, Alberta, T1A 8K6, Canada*

³ *Waterloo CFD Engineering Consulting Inc., Waterloo, Ontario, N2T 2N7, Canada*

Email: fslien@uwaterloo.ca

ABSTRACT

The release of chemical, biological, radiological, or nuclear (CBRN) agents by terrorists or rogue states in a North American city (densely populated urban centre) and the subsequent exposure, deposition, and contamination are emerging threats in an uncertain world. The transport, dispersion, deposition, and fate of a CBRN agent released in an urban environment is an extremely complex problem that encompasses potentially multiple space and time scales. The availability of high-fidelity, time-dependent models for the prediction of a CBRN agent's movement and fate in a complex urban environment can provide the strongest technical and scientific foundation for support of Canada's more broadly based effort at advancing counter-terrorism planning and operational capabilities.

The objective of this paper is to report the progress of developing and validating an integrated, state-of-the-art, high-fidelity multi-scale, multi-physics modeling system for the accurate and efficient prediction of urban flow and dispersion of CBRN materials. Development of this proposed multi-scale modeling system will provide the real-time modeling and simulation tool required to predict injuries, casualties, and contamination and to make relevant decisions (based on the strongest technical and scientific foundations) in order to minimize the consequences of a CBRN incident based on a pre-determined decision making framework.

1 INTRODUCTION

Atmospheric transport and diffusion models have played an important role in emergency response systems. These models have been developed to reliably and promptly calculate the transport, diffusion, and deposition of toxic chemical, biological, or radiological materials released (either accidentally or deliberately) into the turbulent atmospheric boundary layer over relatively smooth and homogeneous surfaces. In particular, all military and civilian (government and commercial) emergency response models employ either empirical relationships based on similarity theory for the mean wind flow and turbulence in the boundary-layer, or use simple diagnostic wind fields that are obtained by extrapolation and/or interpolation of sparse observational data. The advantages of these approaches for wind flow specification required to "drive" dispersion models are their simplicity, general applicability in simple atmospheric conditions, and most importantly, their limited computational demands. While this approach is useful for a landscape that is approximately flat and unobstructed, it is wholly inadequate for surface-atmosphere interactions over "complex" surfaces (i.e., most of the real world) such as cities and other built-up areas.

To address the urgent problem of modeling of the dispersion of CBRN agents in the urban complex, characterized by extremely diverse length and time scales and complex geometries and interfaces, we require physically-based urban wind models that will be able to provide the needed spatial pattern of urban wind statistics. In this study, we report progress in the de-

velopment of a high-fidelity multi-scale, multi-physics modeling system for the accurate and efficient prediction of urban flow and dispersion of CBRN materials. The outline of this paper is as follows. Section 2 summarizes the dispersion models used to predict both continuous and instantaneous releases of contaminant material. The drag-force approach will be presented in Section 3 whereby groups of buildings in the array are aggregated into a number of ‘drag units’ with the ensemble of units treated simply as a spatially continuous porous medium for the prediction of the time-mean spatially-averaged statistics of the mean flow and turbulence in the urban complex. The numerical framework underlying the urban microscale flow model (urbanSTREAM) is described in Section 4. Section 5 addresses work in progress which is summarized in four sub-sections which deal, respectively, with Large-Eddy Simulation (LES) and its variants, the inverse source determination problem, adaptive mesh refinement (AMR), and coupling urbanSTREAM to a mesoscale flow model. Finally, Section 6 contains conclusions.

2 DISPERSION MODELING

The governing equations of mass, momentum, and concentration (of a passive scalar) for incompressible and neutrally-stratified fluid flow based on the Reynolds-averaged Navier-Stokes (RANS) approach are

$$\frac{\partial \bar{u}_j}{\partial x_j} = 0, \quad (1)$$

$$\frac{\partial \bar{u}_i}{\partial t} + \frac{\partial}{\partial x_j} \bar{u}_j \bar{u}_i = -\frac{\partial \bar{p}}{\partial x_i} + \frac{\partial}{\partial x_j} \left(\nu \frac{\partial \bar{u}_i}{\partial x_j} \right) - \frac{\partial}{\partial x_j} \overline{u'_i u'_j}, \quad (2)$$

$$\frac{\partial \bar{c}}{\partial t} + \frac{\partial}{\partial x_j} \bar{u}_j \bar{c} = \frac{\partial}{\partial x_j} \left(D \frac{\partial \bar{c}}{\partial x_j} \right) - \frac{\partial}{\partial x_j} \overline{u'_j c'} + S, \quad (3)$$

where an overbar denotes the Reynolds averaging of a quantity and a prime on a quantity is used to denote the departure of that quantity from its Reynolds-averaged value. Here, \bar{u}_i is the mean velocity in the x_i -direction, t is time, \bar{p} is the kinematic pressure, ν is the kinematic viscosity, \bar{c} is the mean concentration of the passive scalar, D is the molecular diffusivity of the scalar, and S is the source density distribution of the tracer. Unless otherwise noted, the x_i -direction with $i=1, 2$, or 3 will be used to represent the streamwise x , spanwise y , or vertical z directions, respectively; and, u , v , and w will be used to denote the velocity components in the x -, y -, and z -directions, respectively.

Within the framework of the standard (high-Re) k - ϵ model, the Reynolds stresses $\overline{u'_i u'_j}$ and the turbulent scalar fluxes $\overline{u'_j c'}$, required to close the transport equations for the mean momentum and mean concentration, are modeled using the gradient diffusion hypothesis as follows:

$$\overline{u'_i u'_j} = \frac{2}{3} k \delta_{ij} - \nu_t \left(\frac{\partial \bar{u}_i}{\partial x_j} + \frac{\partial \bar{u}_j}{\partial x_i} \right), \quad (4)$$

and

$$\overline{u'_j c'} = -\frac{\nu_t}{\sigma_c} \frac{\partial \bar{c}}{\partial x_j}, \quad (5)$$

where $\nu_t \equiv C_\mu k^2 / \epsilon$ is the kinematic eddy (or, turbulent) viscosity, $C_\mu = 0.09$ is a model (closure) constant, $\sigma_c = 0.63$ is the turbulent Schmidt number, $k \equiv \overline{u'_i u'_i} / 2$ is the turbulence kinetic energy, ϵ is the dissipation rate of turbulence kinetic energy, and δ_{ij} is the Kronecker delta function.

The transport equations for the turbulence quantities k and ϵ are

$$\frac{\partial k}{\partial t} + \frac{\partial}{\partial x_j} \bar{u}_j k = \frac{\partial}{\partial x_j} \left(\frac{\nu_t}{\sigma_k} \frac{\partial k}{\partial x_j} \right) + P_k - \epsilon, \quad (6)$$

$$\frac{\partial \epsilon}{\partial t} + \frac{\partial}{\partial x_j} \bar{u}_j \epsilon = \frac{\partial}{\partial x_j} \left(\frac{\nu_t}{\sigma_\epsilon} \frac{\partial \epsilon}{\partial x_j} \right) + \frac{\epsilon}{k} (C_{\epsilon 1} P_k - C_{\epsilon 2} \epsilon), \quad (7)$$

where $\sigma_k = 1.0$, $\sigma_\epsilon = 1.3$, $C_{\epsilon 1} = 1.44$, and $C_{\epsilon 2} = 1.92$ are model (closure) constants, and the turbulence kinetic energy production term P_k in Eq. (6) is defined as $P_k \equiv -\overline{u'_i u'_j} \frac{\partial \bar{u}_i}{\partial x_j}$

The transport equation for the concentration variance $\overline{c'^2}$ of a passive scalar can be written as

$$\begin{aligned} \frac{\partial \overline{c'^2}}{\partial t} + \frac{\partial}{\partial x_j} \bar{u}_j \overline{c'^2} &= \frac{\partial}{\partial x_j} \left(D \frac{\partial \overline{c'^2}}{\partial x_j} - \overline{u'_j c'^2} \right) \\ &\quad - 2 \overline{u'_j c'} \frac{\partial \bar{c}}{\partial x_j} - \epsilon_c, \end{aligned} \quad (8)$$

where ϵ_c is the scalar variance dissipation rate defined by $\epsilon_c \equiv 2D \frac{\partial \overline{c'}}{\partial x_j} \frac{\partial \overline{c'}}{\partial x_j}$. As in the transport equation for the mean concentration (advection-diffusion equation), the turbulent flux of concentration variance is modeled using the gradient diffusion approach as

$$\overline{u'_j c'^2} = -\frac{\nu_t}{\sigma_c} \frac{\partial \overline{c'^2}}{\partial x_j}. \quad (9)$$

The critical term in the closure of the transport equation of the concentration variance [cf. Eq. (8)] is ε_c which represents the dissipation of $\overline{c'^2}$ by molecular diffusion in the fine-scale scalar structure. This is a term responsible for micromixing of the scalar and, as such, corresponds to a small-scale term controlled by the scalar gradient correlations. This term will be modeled algebraically using an expression with the general form $\varepsilon_c = \overline{c'^2}/t_d$, where t_d is an appropriately defined dissipation time scale that is characteristic of the decay time of the concentration fluctuations in the scalar field. In the present study, two models are used to describe the scalar dissipation time scale.

Model 1: In this model,

$$\varepsilon_c = C_\chi \frac{\varepsilon}{k} \overline{c'^2} \quad (10)$$

where C_χ is a model constant that represents the ratio of the turbulence integral time scale to the scalar dissipation time scale. In the present study, we will use $C_\chi = 2$, as suggested by [5] in our simulations of the scalar variance field.

Model 2: In this model,

$$\varepsilon_c = C_\chi \frac{k^{1/2} \overline{c'^2}}{\Lambda_d} \quad (11)$$

where Λ_d is the dissipation length scale in the dispersing plume or cloud (puff). Equivalently, in this model, t_d is proportional to $\Lambda_d/k^{1/2}$. In the present study, we propose to use a simple algebraic formulation for the dissipation length scale; namely,

$$\Lambda_d = [\sigma_y(x)\sigma_z(x)]^{1/2} \quad (\text{for a plume}), \quad (12)$$

and

$$\Lambda_d = [\sigma_x(t)\sigma_y(t)\sigma_z(t)]^{1/3} \quad (\text{for a cloud or puff}), \quad (13)$$

where σ_x , σ_y , and σ_z are the plume or puff spreads (standard deviations) of the mean concentration distribution in the x -, y -, and z -directions, respectively. The closure constant C_χ is equal to 1.25 and 2.1 for a plume and cloud (puff), respectively. These values for C_χ were chosen to give the best conformance with the available data for the MUST array, and in particular, were chosen to ensure the best fit to the decay of the plume or cloud centreline fluctuation intensity (ratio of the concentration standard deviation to the mean concentration) with downstream distance from the source.

Fig. 1 shows the geometry of the Mock Urban Setting Test (MUST) array [19] and source location. This full-scale atmospheric experiment was replicated at a scale of 1:205 in a boundary-layer water channel by Coanda Research & Development Corporation (Burnaby, BC, Canada). Sample results for the instantaneous release (puff) case only, obtained with a $203 \times 45 \times 43$ grid, are given in Fig. 2 in terms of the vertical profiles of streamwise velocity \bar{u} at $y = 0$ (vertical centre plane of the array) and the horizontal profiles of total dosage at $z/H = 0.75$ (H is the height of the obstacles) at the 6.5 row location. Fig. 2 also shows time histories of normalized mean concentration (\bar{c}/c_s) and normalized concentration standard deviation (c'_{rms}/c_s) profiles at $y/H = 0$, $z/H = 0.75$ at the 6.5 row location. The total dosage is defined as

$$\text{dose} = \int_0^T \bar{c} dt, \quad (14)$$

where T is a time interval that is chosen to be sufficiently long so as to include the duration (time interval) between the arrival time and departure time of the cloud (puff) at the given receptor location where the dosage is calculated (or, measured). As seen, excellent agreement between the predicted and measured \bar{u} -profiles is achieved. Fig. 2 also shows that the time history of \bar{c}/c_s and the profile of horizontal dosage are reasonably well predicted by solving a simple advection-diffusion equation (Eq. 3). In the case of c'_{rms}/c_s prediction, Model 2 is clearly better than Model 1 and is therefore recommended in the present study.

3 DRAG-FORCE APPROACH

3.1 Model Formulation

The turbulent flow within and over urban areas covered with agglomerations of discrete buildings, often with irregular geometry and spacing, is generally very complex and possesses a fully three-dimensional structure. Although the application of CFD to the prediction of the mean flow and turbulence near and around a single building or within and over a regular array (or, canopy) of buildings is progressing, this method tends to require extensive computational resources.

Here, we focus on the formulation of a numerical model for the prediction of flows within and over a building array based on an aggregation of groups of

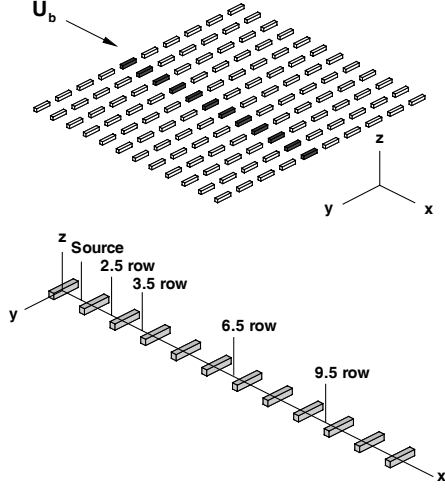


Figure 1: A 3-D perspective view of the MUST obstacle array.

buildings in the array into a number of ‘drag units’, with each unit being treated as a porous barrier. This approach will obviate the need to impose boundary conditions along the surfaces of all buildings (and other obstacles) in the urban complex. Before we begin, we present a short note on the notation that will be used. For any flow variable ϕ , $\langle \phi \rangle$ will denote the spatial (volume) average, $\bar{\phi}$ the time average, ϕ' the departure of ϕ from its time-averaged value, and ϕ'' the departure of ϕ from its spatially-averaged value. With the assumption that

$$\langle u_i'' u_j'' \rangle \ll \langle u_i' \rangle \langle u_j' \rangle \quad (15)$$

(i.e., the dispersive stresses can be ignored) and

$$\overline{\langle u_i' \rangle \langle u_j' \rangle} = \frac{2}{3} \delta_{ij} \bar{\kappa} - v_t \left(\frac{\partial \langle \bar{u}_i \rangle}{\partial x_j} + \frac{\partial \langle \bar{u}_j \rangle}{\partial x_i} \right), \quad (16)$$

where $\bar{\kappa}$, ε and v_t are defined as

$$\bar{\kappa} \equiv \frac{1}{2} \overline{\langle u_i' \rangle \langle u_i' \rangle}, \quad \varepsilon \equiv v \frac{\partial \langle u_i' \rangle}{\partial x_k} \frac{\partial \langle u_i' \rangle}{\partial x_k}, \quad v_t = C_\mu \frac{\bar{\kappa}^2}{\varepsilon}, \quad (17)$$

the modeled time-averaged, spatially-averaged Navier-Stokes (NS) equation can be written as

$$\begin{aligned} \frac{\partial \langle \bar{u}_j \rangle \langle \bar{u}_i \rangle}{\partial x_j} &= -\frac{\partial \langle \bar{p} \rangle}{\partial x_i} \\ &+ \frac{\partial}{\partial x_j} \left[(v + v_t) \left(\frac{\partial \langle \bar{u}_i \rangle}{\partial x_j} + \frac{\partial \langle \bar{u}_j \rangle}{\partial x_i} \right) - \frac{2}{3} \delta_{ij} \bar{\kappa} \right] \\ &- C_{DA} \left[\left(Q + \frac{2}{3} \frac{\bar{\kappa}}{Q} \right) \langle \bar{u}_i \rangle - v_t \left(\frac{\partial \langle \bar{u}_i \rangle}{\partial x_j} + \frac{\partial \langle \bar{u}_j \rangle}{\partial x_i} \right) \frac{\langle \bar{u}_j \rangle}{Q} \right], \end{aligned} \quad (18)$$

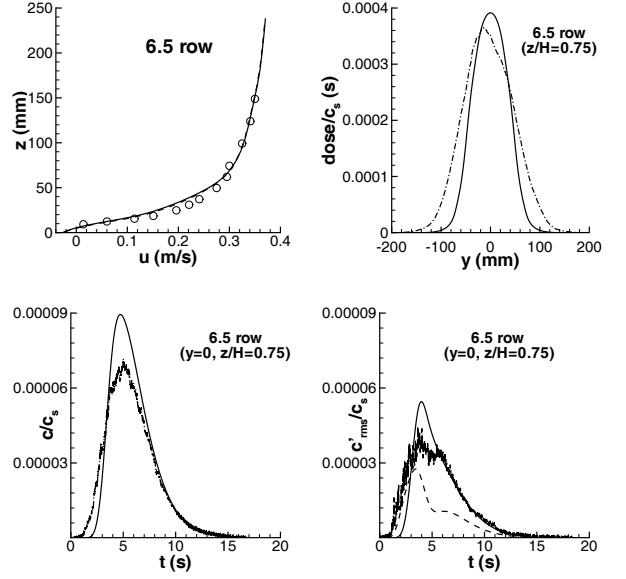


Figure 2: Vertical velocity profiles at $y/L = 0$, horizontal dosage profiles at $z/H = 0.75$ and time histories of \bar{c}/c_s and c'_{rms}/c_s , at $y/L = 0$, $z/H = 0.75$ at the 6.5 row location. For the top two panels and the bottom left panel: $-\cdot-\cdot-$, \circ Experimental data; $—$ Model prediction. For the bottom right panel: $-\cdot-\cdot-$ Experimental data; $----$ Model prediction for concentration standard deviation using Model 1 for ε_c ; $—$ Model prediction for concentration standard deviation using Model 2 for ε_c . Here, L and H are the streamwise length and height of the obstacles, respectively.

with $Q \equiv (\langle \bar{u}_i \rangle \langle \bar{u}_i \rangle)^{1/2}$ being the magnitude of the spatially-averaged, time-mean wind speed.

The transport equations for $\bar{\kappa}$ and ε can be modeled in the following the form [see [10] for details]:

$$\frac{\partial \langle \bar{u}_j \rangle \bar{\kappa}}{\partial x_j} = \frac{\partial}{\partial x_j} \left(\frac{v_t}{\sigma_k} \frac{\partial \bar{\kappa}}{\partial x_j} \right) + (P + F) - \varepsilon, \quad (19)$$

$$\begin{aligned} \frac{\partial \langle \bar{u}_j \rangle \varepsilon}{\partial x_j} &= \frac{\partial}{\partial x_j} \left(\frac{v_t}{\sigma_\varepsilon} \frac{\partial \varepsilon}{\partial x_j} \right) \\ &+ \frac{\varepsilon}{\bar{\kappa}} (C_{\varepsilon 1} (P + F) - C_{\varepsilon 2} \varepsilon), \end{aligned} \quad (20)$$

where $P \equiv -\overline{\langle u'_i \rangle \langle u'_j \rangle} \frac{\partial \langle \bar{u} \rangle}{\partial x_j}$ is the production term, and

$$F = -C_D \hat{A} \left[2Q\bar{\kappa} + \frac{1}{Q} \left(\langle \bar{u} \rangle \langle \bar{u}_k \rangle \overline{\langle u'_i \rangle \langle u'_k \rangle} \right) + \frac{1}{Q} \left(\langle \bar{u}_k \rangle \overline{\langle u'_i \rangle \langle u'_k \rangle} \right) \right]. \quad (21)$$

The triple correlation term $\overline{\langle u'_i \rangle \langle u'_j \rangle \langle u'_k \rangle}$ in Eq. (21) can be modeled as

$$\overline{\langle u'_i \rangle \langle u'_j \rangle \langle u'_k \rangle} = 2C_s \frac{\bar{\kappa}}{\varepsilon} \left[\frac{\langle u'_k \rangle \langle u'_j \rangle}{\partial x_l} \frac{\partial \bar{\kappa}}{\partial x_l} + \overline{\langle u'_i \rangle \langle u'_j \rangle} \frac{\partial \langle u'_k \rangle}{\partial x_l} \right]. \quad (22)$$

The empirical (closure) constants in Eqs. (17), (19), (20), and (22) are

$$C_\mu = 0.09, \quad \sigma_k = 1, \quad \sigma_\varepsilon = 1.3, \\ C_{\varepsilon 1} = 1.44, \quad C_{\varepsilon 2} = 1.92, \quad C_s = 0.3. \quad (23)$$

3.2 Determination of Drag Coefficient

In this section, we explicitly diagnose a drag coefficient C_D using the results from a high-resolution CFD simulation of a developing flow over an aligned array of cubes (3-D buildings) shown in Fig. 3. This array consists of seven rows of cubes arranged with a plan area density, λ_P , of 0.25 and a frontal area density, λ_F , of 0.25 [2]. Excellent agreement of the predicted \bar{u} -profile with the experimental data and good conformance between the predicted k values and the corresponding measurements were reported in [11].

To derive a drag coefficient for this array, the following formula was proposed:

$$C_D(z)\hat{A} = \frac{-\bar{f}_x}{\max(\delta, Q\langle \bar{u} \rangle(z))}, \quad (24)$$

where

$$\bar{f}_x \equiv \frac{\nu}{V} \int_S \frac{\partial \bar{u}}{\partial n} dS - \frac{1}{V} \int_S \bar{p} n_x dS \quad (25)$$

and $\delta \approx 0.0025 \ll 1$ is chosen here to avoid a possible singularity problem for the case when $\langle \bar{u} \rangle \approx 0$. Both surface integrals in Eq. 25 can be evaluated explicitly using the high-resolution CFD results and the resulting $C_D(z)$ over the range of heights $0 \leq z/H \leq 1$ for each drag unit in the 3-D building array are shown in Fig. 4.

Although C_D for a regular array can be determined rigorously, it is a common practice to use empirical formulae (for example, as proposed in [13]) when a real city such as that shown in Fig. 5 is to be simulated.

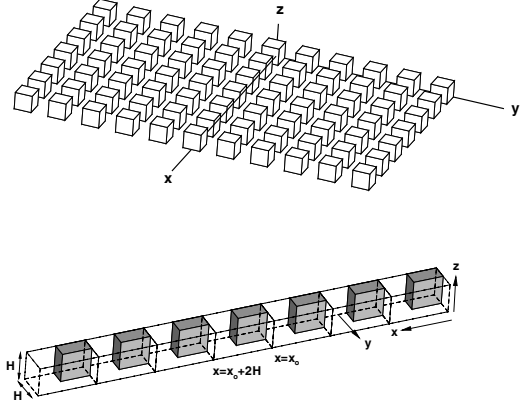


Figure 3: A 3-D perspective view of the aligned array of cubes (top) and the corresponding ‘drag unit’ (bottom).

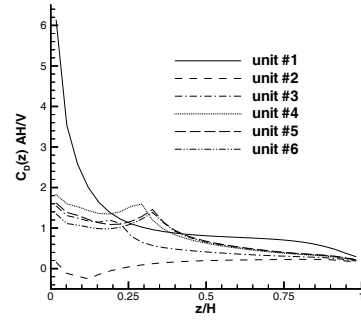


Figure 4: The variation of $C_D(z)\hat{A}$ for each drag unit [12].

4 NUMERICAL FRAMEWORK FOR URBANSTREAM

The urbanSTREAM code developed for the present study is based on a fully collocated, finite-volume CFD code STREAM [8], which solves the coupled system of partial differential equations that model the three-dimensional flow, turbulence and concentration

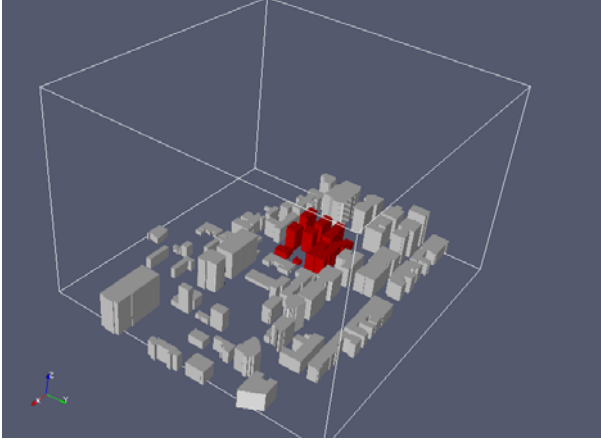


Figure 5: Sample buildings in the city of Ottawa.

fields. Within a non-orthogonal system, the velocity vector is decomposed into its Cartesian components, and these are the components to which the momentum equations relate. Diffusive volume-face fluxes are discretized using a second-order accurate central differencing scheme. Advective volume-face fluxes are approximated using a second-order accurate total-variation-diminishing (TVD) scheme referred to as the Upstream Monotonic Interpolation for Scalar Transport (UMIST) limiter [9]. The transient term is discretized using a fully implicit, second-order accurate three-time-level method. The SIMPLEC algorithm was used for pressure correction and the widely used method of Rhie and Chow [16] was adopted to non-linearly interpolate the cell face velocities from the nodal values (at the centres of the cells) in order to avoid checkerboard oscillations in the pressure field, reflecting a state of pressure-velocity decoupling.

5 WORK IN PROGRESS

5.1 Large-Eddy Simulation (LES)

5.1.1 Conventional LES

When the Navier-Stokes and continuity equations for incompressible flow are filtered, one obtains

$$\frac{\partial \bar{u}_i}{\partial x_i} = 0, \quad (26)$$

$$\frac{\partial \bar{u}_i}{\partial t} + \frac{\partial \bar{u}_i \bar{u}_j}{\partial x_j} = -\frac{1}{\rho} \frac{\partial \bar{p}}{\partial x_i} - \frac{\partial}{\partial x_j} \underbrace{(\bar{u}_i \bar{u}_j - \bar{u}_i \bar{u}_j)}_{\tau_{ij}}, \quad (27)$$

where \bar{u}_i denotes the spatially filtered velocity components with \bar{u}_1 in the streamwise $x_1 \equiv x$, \bar{u}_2 in the wall-normal $x_2 \equiv y$, and \bar{u}_3 in the spanwise $x_3 \equiv z$ directions, respectively; \bar{p} is the filtered pressure; and, ρ is the fluid density. In the context of LES, τ_{ij} in Eq. (27) is the subgrid-scale (SGS) stress tensor that is associated with the large-scale (resolved) momentum flux caused by the action of the small (unresolved) scales, and as such needs to be modeled. The most common class of subgrid models for τ_{ij} is an eddy viscosity type with the following form:

$$\tau_{ij} - \frac{1}{3} \tau_{kk} \delta_{ij} = \nu_{\text{sgs}} \left(\frac{\partial \bar{u}_i}{\partial x_j} + \frac{\partial \bar{u}_j}{\partial x_i} \right) \equiv -2\nu_{\text{sgs}} \bar{S}_{ij}, \quad (28)$$

where ν_{sgs} is the subgrid-scale viscosity determined from

$$\nu_{\text{sgs}} = C \bar{\Delta}^2 |\bar{S}|. \quad (29)$$

Here, $\bar{\Delta}$ is the filter length scale, $|\bar{S}| \equiv (2\bar{S}_{ij}\bar{S}_{ij})^{1/2}$ and C is the model parameter. A number of different methods have been used to specify C , including the standard Smagorinsky model (SMG), the dynamic model with time averaging (DMT) [1], and the localized dynamic method (LDM) [15].

The geometry of the obstacle array is exhibited in Fig. 6. To simulate the flow in this array, we used a computational domain consisting of a sub-channel unit shown in Fig. 6. This sub-channel unit had dimensions of $4H \times 3.4H \times 4H$ for the LES calculations with $48 \times 48 \times 48$ grid points, and $4H \times 3.4H \times 2H$ for the RANS calculations with $81 \times 60 \times 47$ grid points in the streamwise x -, wall-normal y -, and spanwise z -directions, respectively. A side view of the sub-channel unit showing 5 measurement locations is sketched in Fig. 6 (bottom) in accordance with [14].

Profiles of streamwise velocity \bar{u} on a horizontal (x - z) plane at half cube height (i.e., at $y/H = 0.5$), and profiles of spanwise Reynolds normal stress $\overline{w'w'}$ on the vertical plane through the centre of the cube (i.e., at $z/H = 0$) at five stations obtained with RANS (using the standard k - ϵ turbulence model) and three LES variants are shown in Fig. 7. It is seen clearly that LES is better than RANS, in particular, in terms of predictions of the horizontal profiles of \bar{u} . However, the differences between SMG, DMT and LDM are reasonably small (details can be found in [4]).

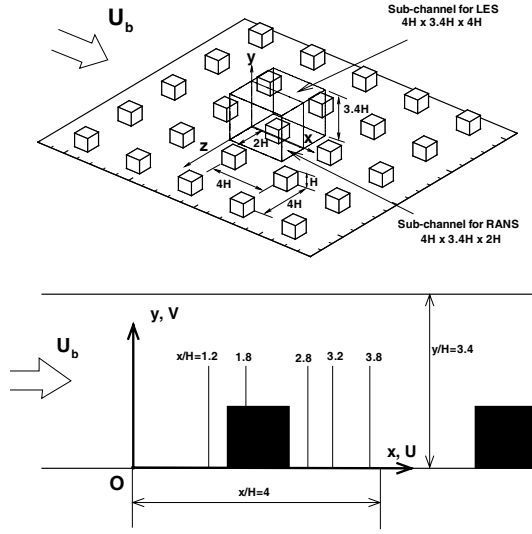


Figure 6: The geometry of obstacle array and a side view of the sub-channel unit showing measurement locations.

5.1.2 Hybrid RANS/LES

The basic idea of the hybrid RANS/LES approach is to resolve the large scales of turbulence in regions away from walls using LES and model the unresolved scales using RANS in the near-wall regions so that a good compromise between accuracy and efficiency can be achieved. One successful example, belonging to this category, is the Detached Eddy Simulation (DES) [18] when applied to a high-lift airfoil at a high angle of attack. Although the lift curve (an integral quantity) is fairly well predicted, the turbulence structure within the boundary layers may not be. In fact, several recent studies for a fully developed channel flow using the hybrid RANS/LES approach have shown that, due to the incompatibility between the two regions (namely, spatial filtering in the LES region and time or ensemble averaging in the RANS region), an artificial buffer-like layer often occurs at the interface location as shown by the curve labeled with “Hybrid” in Fig. 8; viz., the velocity gradient $\partial \bar{u} / \partial y$ increases suddenly across the interface on the LES side. One possible remedy for this problem is to introduce a forcing term, based on velocity fluctuations extracted from a pre-computed DNS database or generated as a random perturbation, into the momentum equation. The basic idea can be illus-

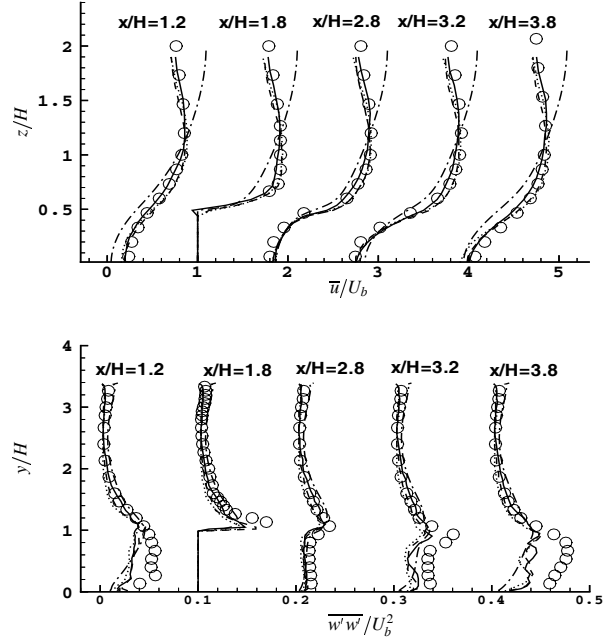


Figure 7: Profiles of streamwise velocity on the horizontal (x - z) plane at half cube height, and profiles of spanwise Reynolds normal stress on the vertical plane through the centre of the cube. — LDM; --- DMT; SMG; —·— RANS; ○ EXP.

trated by the following average streamwise momentum equation

$$(v + v_t) \frac{\partial \bar{u}}{\partial y} - \overline{u'v'} = u_t^2 (1 - y). \quad (30)$$

The effect of the forcing term, introduced in the vicinity of the interface location (more on the LES side), is to increase v_t and, as a result, to reduce $\partial \bar{u} / \partial y$ (see curve labeled with “Hybrid+Force” in Fig. 8). Details can be found in [7].

5.1.3 Partially Resolved Numerical Simulation (PRNS)

As discussed in Section 5.1.2, the occurrence of a non-physical buffer-like layer in the vicinity of the interface location when hybrid RANS/LES is adopted is due to flow quantities in the RANS and LES regions being defined differently: namely, quantities in the LES region are based on spatial filtering whereas those in the

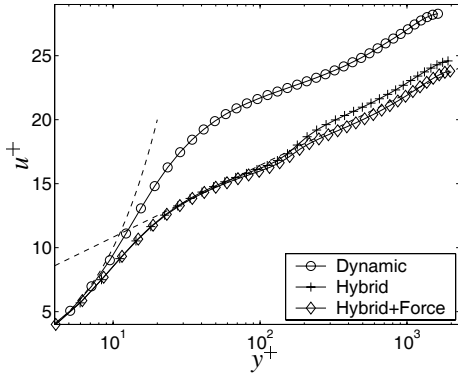


Figure 8: Streamwise velocity profiles in wall units (viz., $y^+ = yu_\tau/\nu$) for a fully-developed channel flow.

RANS region is based on statistical averaging. There is a need to develop a unified approach so that RANS, URANS, LES and DNS can be put into the same category. This can be achieved when the NS equations are filtered in time, rather than space, as advocated by Shih & Liu [17] in their PRNS formulation. If the cut-off frequency, f_c , of the temporal filter is set to zero, PRNS becomes RANS; if the cutoff frequency f_c is set to the reciprocal of the Kolmogorov time scale t_K (i.e., $f_c = 1/t_K \equiv 1/\sqrt{\nu/\epsilon}$), PRNS reduces to DNS. For URANS and LES, f_c of the temporal filter must be chosen to lie at the range of frequencies corresponding to the energy-containing and inertia subrange scales of turbulence, respectively. If the two-equation k - ϵ turbulence model is used as the basis for the PRNS framework, the generalized turbulent viscosity

$$\nu_t = \mathcal{F}_{RCP}(f_c) C_\mu \frac{k^2}{\epsilon} \quad (31)$$

defines a generalized turbulence model that can be interpreted as a combination of an eddy viscosity model as used in RANS or a subgrid scale model as used in LES. Here, $\mathcal{F}_{RCP}(f_c)$ is a resolution control parameter function of f_c that rescales the eddy viscosity in accordance to the degree of temporal filtering imposed on the NS equations. Although the precise functional form for $\mathcal{F}_{RCP}(f_c)$ has yet to be determined, it can be readily seen that for RANS and URANS, $\mathcal{F}_{RCP} \rightarrow 1^-$ (as $f_c \rightarrow 0^+$) and for DNS, $\mathcal{F}_{RCP} \rightarrow 0^+$ (as $f_c \rightarrow 1/t_K$). The hope here is to obtain a generalized subgrid scale model which is capable of handling coarse grids similar to those used in URANS computations for LES for cases where it is necessary (owing to computational cost) to locate the cutoff of the temporal filter in the

low-frequency portion of the turbulence energy spectrum (or, near the beginning of the inertial subrange in the energy spectrum).

To illustrate the application of PRNS, calculations were performed for the disturbed flow over a regular (aligned) array of 16×16 obstacles, each with a square cross-section of side length H and height $2H$. This obstacle array with frontal and plan area densities of 0.5 and 0.25, respectively, is shown in Fig. 9. As seen in Fig. 10, both RANS and PRNS predict the streamwise mean velocity profiles extremely well. However, for turbulence kinetic energy levels within the array, PRNS performs much better in comparison with the experimental data than RANS.

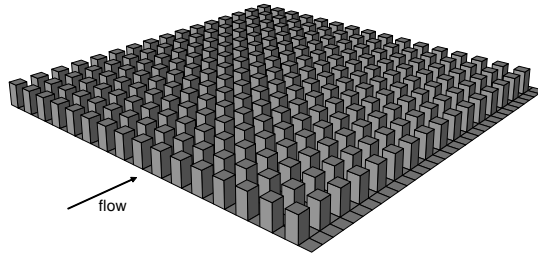


Figure 9: A regular and aligned array of obstacles, each with a square cross-section of side length H and height $2H$.

5.1.4 Monotonically Integrated LES (MILES)

The main challenge for the conventional LES is to ensure that numerical viscosity is much less than the SGS viscosity in order to assess the true performance of SGS models. The common practice is to adopt the central difference scheme (CDS) for advection. However, in order to avoid spurious oscillations when the cell Peclet number is greater than two, a fine grid is usually required. If the numerical viscosity is comparable to the SGS viscosity in the sense that it *alone* is sufficient to “drain” the energy generated by the energy-containing scales of turbulence, then an explicit SGS model is not required. This is the basic idea of the MILES approach and its theoretical analysis within the framework of flux-limiting finite-volume discretizations can be found in [3]. Here, the emphasis is placed on the relationship between the leading-order numerical (truncation) errors and the implicit SGS models implied by these errors. In the present study, the UMIST

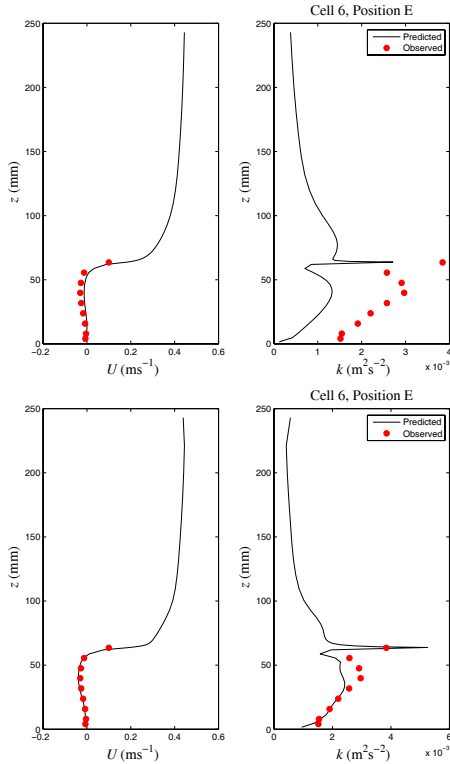


Figure 10: Vertical profiles of streamwise mean velocity and turbulence energy predicted and measured at position E in a unit cell located in the sixth row of obstacles in the array. Position E lies in the wake region behind the obstacle. The top row of panels show the results for (steady-state) RANS and the bottom row of panels show the results for PRNS with $\mathcal{F}_{\text{RCP}}(f_c) = 5/9$. — Predicted; \circ EXP.

limiter [9] is adopted for the discretization of the non-linear convective term.

Preliminary results obtained with a fairly coarse grid of $27 \times 25 \times 32$ nodes for the obstacle array shown in Fig. 6 is given in Fig. 11. Interestingly, there is reasonably good conformance between the predicted spanwise Reynolds normal stresses and the experimental measurements for the three x/H locations as seen in Fig. 11. This agreement is comparable to that obtained using a conventional LES with an explicit dynamic SGS model [cf. Fig. 7]. More importantly, the grid for the sub-domain used here is rather coarse. If we scale it up to simulate a developing flow over the regular array of 16×16 obstacles shown in Fig. 9, a

tal of more than 5.5×10^6 nodes will be required. The implication of this is that MILES is probably the most viable and efficient approach for the LES simulation of urban canopy flows simply because the grid resolution affordable to each building is very limited.

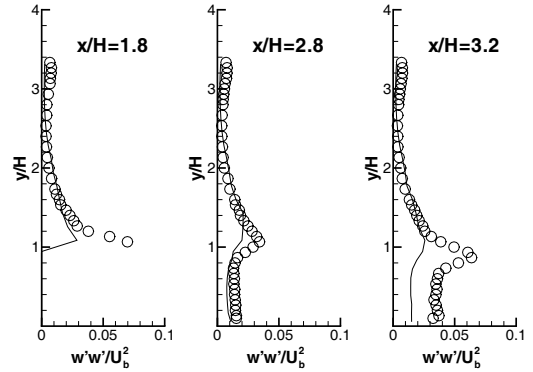


Figure 11: Profiles of spanwise Reynolds normal stress in the vertical (x - y) plane through the centre of the cube (i.e., at $z/H = 0$): — MILES; \circ EXP.

5.2 Inverse Source Determination

5.2.1 Mathematical Formulation

The inverse source determination problem is generally an ill-posed problem with no unique solution. To solve this ill-posed problem, it is necessary to formulate an approach that (1) incorporates *a priori* information on the possible solutions in a cogent manner and (2) incorporates quantitatively the lack of total precision in the problem due to measurement noise and model (and input) uncertainties. Hence, the inverse source problem is a problem of inductive logic (or inference) rather than deductive logic. Probability theory when interpreted as logic is a quantitative theory of inference, just as mathematics is a quantitative theory of deduction.

The rational framework for the formulation of the inverse source problem is to apply Bayesian probability theory. To this purpose, the application of Bayes' theorem to the inverse source determination problem takes

the following form:

$$p(m|D, I) \propto \underbrace{p(m|I)}_{\text{prior}} \underbrace{p(D|m, I)}_{\text{likelihood}}, \quad (32)$$

where $p(m|D, I)$ is the posterior probability density function (PDF) for m (source function), I denotes all the background information available to the observer (e.g., meteorology, position of detectors, dispersion model), and D are the concentration data provided by the detectors. The posterior PDF for m is proportional to the product of the prior PDF for m , $p(m|I)$, and the likelihood function, $p(D|m, I)$. The prior PDF $p(m|I)$ encodes all the information available about the putative source before the receipt of the concentration data D . The likelihood function, $p(D|m, I)$, is the PDF for observing the data D (i.e., measured concentration data) under ‘‘hypothesis’’ m (given source distribution), accounting for (1) model errors and input errors in the theoretical source-receptor relationship between the observed concentration and source distribution, and (2) uncertainty arising from the measurement noise in the detector. Assume the i -th concentration datum is measured subject to an additive Gaussian noise with root-mean-square (RMS) experimental error $\sigma_{D,i}$ and that the modeling error for the concentration datum has a Gaussian RMS error $\sigma_{T,i}$ (expected error in the model prediction of the concentration datum given a source model m). Furthermore, it is assumed that the measurement and modeling errors are statistically independent. Then the likelihood function reduces to

$$p(D|m, I) \propto \exp \left[-\frac{1}{2} (D - R(m))^t \Sigma^{-1} (D - R(m)) \right], \quad (33)$$

where

$$\Sigma = \text{diag} \{ \sigma_{D,i}^2 + \sigma_{T,i}^2 \}_{i=1}^N. \quad (34)$$

Here, R is the theoretical source-receptor relationship and N is the number of concentration data. In assigning the prior probability $p(m|I)$, exactly what is known about the source function m will have to be stated. Assuming that nothing is known about the source parameters (e.g., source location and strength) we have $p(m|I) = \text{constant}$, and the posterior probability density function for the source parameters in this case is given by

$$p(m|D, I) \propto \exp \left[-\frac{1}{2} \sum_{i=1}^N \frac{(C(\vec{x}_i) - R_i(m))^2}{\sigma_{D,i}^2 + \sigma_{T,i}^2} \right], \quad (35)$$

where $C(\vec{x}_i)$ denotes the measured time-averaged concentration for the detector at location \vec{x}_i . To calculate

the posterior probability, we must explicitly specify a model $R(m)$ (dispersion model) relating the source parameters to the concentration observed at the receptor locations; viz., the model concentration C_m at receptor location \vec{x}_r is given by $C_m(\vec{x}_r) = R_r(m)$.

In order to efficiently calculate the source-receptor relationship, the following duality relation is used:

$$(C, h) = (C^*, Q_s), \quad (36)$$

where the inner product of f and g is defined as $(f, g) \equiv \int_{\Omega} f g d\Omega$, h is the receptor response function with units of m^{-3} which embodies the measurement characteristics of a detector (e.g., $h = \delta(\vec{x} - \vec{x}_r)$ for an ideal point detector at receptor location \vec{x}_r) and Q_s with units of $\text{kg m}^{-3} \text{s}^{-1}$ is the source density function. C^* , the residence time density function with units of s m^{-3} , is the dual to the concentration function C and can be obtained by solving the adjoint of the steady-state advection-diffusion equation:

$$-\frac{\partial(\bar{u} C^*)}{\partial x_i} - \frac{\partial}{\partial x_i} \left(\left(D + \frac{v_t}{\sigma_c} \right) \frac{\partial C^*}{\partial x_i} \right) = h \quad (37)$$

subject to the following boundary conditions:

$$\left(D + \frac{v_t}{\sigma_c} \right) \frac{\partial C^*}{\partial n} + \vec{u} \cdot \vec{n} C^* = 0 \quad (38)$$

at the inflow and outflow boundaries of the flow domain, and $\frac{\partial C^*}{\partial z} = 0$ at all solid surfaces (e.g., ground surface, walls and roofs of buildings, etc.) and in the far field.

5.2.2 MUST Array Results

Two different source-receptor configurations are outlined below in Tables 1 and 3, with reference to the MUST array. The posterior PDF was sampled using Metropolis-Hastings Markov chain Monte Carlo; statistical estimates of the source parameters are presented in Tables 2 and 4. In all cases, the source strength for the continuous release is $3.7799 \times 10^{-3} \text{ kg m}^{-3} \text{ s}^{-1}$. The combined RMS experimental and modeling errors, $(\sigma_{D,i}^2 + \sigma_{T,i}^2)^{1/2}$, are assumed to be 10%. In the following two examples, x refers to the streamwise direction, y refers to the vertical direction, and z refers to the spanwise direction. It is clear from the results that the mean and standard deviations of the

	x_s	y_s	z_s
Source location	1.5 row	0.0H	0.0H
Detector positions	4.5 row	0.0H	0.0H
	6.5 row	0.0H	0.0H
	9.5 row	0.0H	0.0H
	12.5 row	0.0H	0.0H
	4.5 row	5.4H	-9.0H
	4.5 row	5.4H	-6.0H
	4.5 row	5.4H	-3.0H
	4.5 row	5.4H	3.0H
	4.5 row	5.4H	6.0H
	4.5 row	5.4H	9.0H

Table 1: Case 1: Source and detector locations

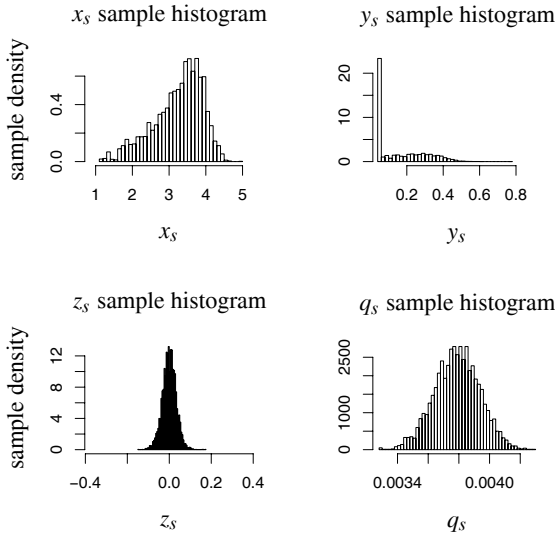


Figure 12: Case 1: Histograms of source parameter samples

	actual	mean	std. dev.
x_s	3.665	3.245	6.684×10^{-1}
y_s	0.0	0.160	1.318×10^{-1}
z_s	0.0	0.000	3.335×10^{-2}
q_s	3.7799×10^{-3}	3.7880×10^{-3}	1.472×10^{-4}

Table 2: Case 1: Source parameter estimates

	x_s	y_s	z_s
Source location	1.5 row	5.4H	-4.0H
Detector positions	4.5 row	0.0H	0.0H
	6.5 row	0.0H	0.0H
	9.5 row	0.0H	0.0H
	12.5 row	0.0H	0.0H
	4.5 row	5.4H	-3.0H
	4.5 row	5.4H	3.0H
	4.5 row	5.4H	0.0H
	4.5 row	5.4H	3.0H
	4.5 row	5.4H	6.0H
	6.5 row	5.4H	0.0H

Table 3: Case 2: Source and detector locations

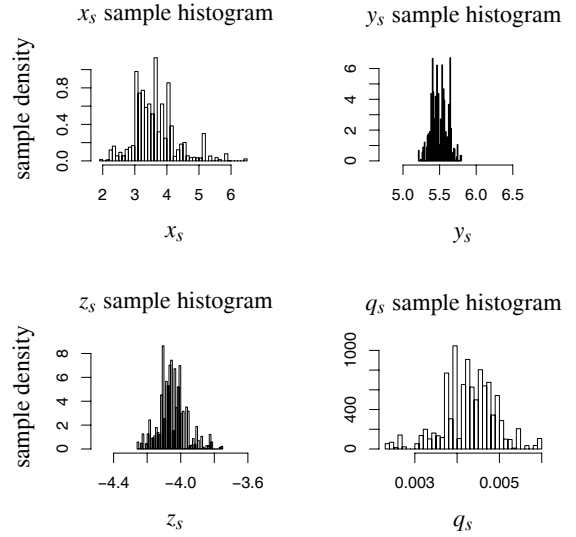


Figure 13: Case 2: Histograms of source parameter samples

	actual	mean	std. dev.
x_s	3.665	3.621	6.573×10^{-1}
y_s	5.382	5.499	1.097×10^{-1}
z_s	-4.032	-4.050	8.171×10^{-2}
q_s	3.7799×10^{-3}	4.2822×10^{-3}	6.202×10^{-4}

Table 4: Case 2: Source parameter estimates

posterior distributions are informative. Adaptive sampling strategies and extra prior information may im-

prove the results, and remain to be investigated.

5.3 Adaptive Mesh Refinement

The fully threaded tree (FTT) for adaptive mesh refinement (AMR) of regular meshes, developed by Khokhlov [6] for high-speed compressible flow involving moving shocks, has been adopted here to further enhance the capability of urbanSTREAM to resolve buildings of different sizes accurately and efficiently in a general urban environment. The main advantages of FTT are low memory overhead relative to the unstructured-grid methods and ease of parallelization. The logical relationships of FTT can be illustrated using a 1-D binary tree shown in Fig. 14. The corresponding quad- (in 2-D) and oct-trees (in 3-D) are similar. The key feature of FTT is that it provides an easy access to every cell, whether a leaf (cell with no children) or, to its children, neighbours and parents; viz., FTT is a tree threaded in all possible directions. Therefore, the neighbour-neighbour relation is not *reciprocal* for leaves of different sizes that face each other. As an example, in Fig. 14 it is seen that cell 5 has cell 3 as its neighbour. However, cell 3 has cell 2 as its neighbour, and not cell 5.

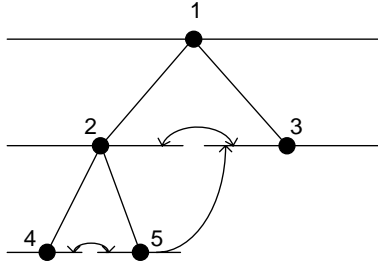


Figure 14: A 1-D binary, fully threaded tree data structure.

The advective and diffusive fluxes at a face with adjacent neighbours of different sizes, as shown in Fig. 15, require special care. For example, if a second-order central difference scheme (CDS) is adopted, the advective velocity u_f is approximated as

$$u_f = \frac{1}{3}(u_{E'} + 2u_P), \quad (39)$$

$$u_{E'} = u_E + \left(\frac{\partial u}{\partial y}\right)_E (y_P - y_E).$$

For the diffusive flux $(\Gamma \nabla \phi \cdot \vec{n})_f$, where Γ is the diffu-

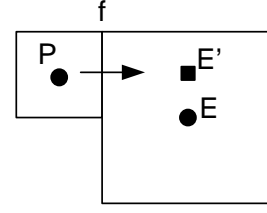


Figure 15: Grid stencil used to approximate advective and diffusive fluxes in AMR.

sivity,

$$(\Gamma \nabla \phi \cdot \vec{n})_f = \Gamma_f \left(\frac{\phi_{E'} - \phi_P}{x_E - x_P} \right), \quad (40)$$

$$\phi_{E'} = \phi_E + \left(\frac{\partial \phi}{\partial y} \right)_E (y_P - y_E).$$

Although standard grid-based matrix solvers cannot be used on a FTT, the multigrid method with the Gauss-Seidel smoother and V-cycle can be used here. The convergence history as a function of work unit for a lid-driven cavity flow at $Re=1000$ is shown in Fig. 16. The velocity vector plot shown in Fig. 17 is on a mesh refined locally based on the criterion that the absolute value of the gradient of velocity magnitude be less than a pre-specified threshold value.

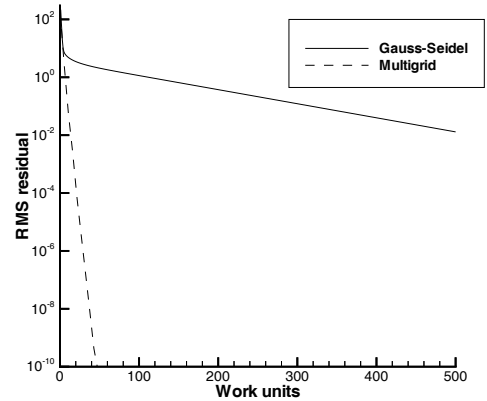


Figure 16: The convergence histories of a single grid (SG) and multigrid (MG) solver for a lid-driven cavity flow.

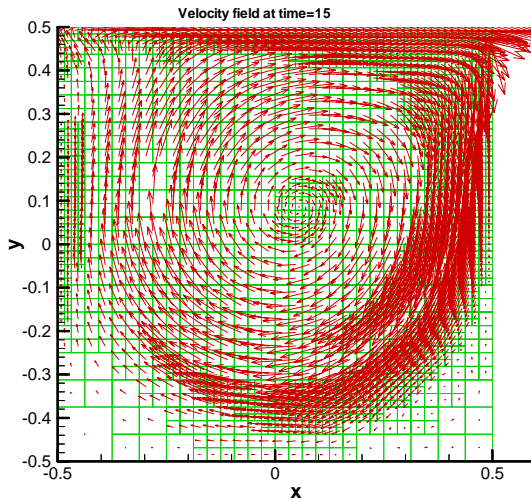


Figure 17: The velocity vector plot on a locally refined mesh for a lid-driven cavity flow.

5.4 Coupling urbanSTREAM With a Mesoscale Flow Model

The interface between urbanSTREAM and the “urbanized” Global Environmental Multiscale/Limited Area Model (GEM/LAM), developed by Environment Canada, is demanding in that the information transfer between the two models must honor physical conservation laws, mutually satisfy mathematical boundary conditions, and preserve numerical accuracy, even though the corresponding meshes might differ in structure, resolution, and discretization methodology. Inter-grid communication allows the coarse mesh solution obtained by GEM/LAM to impose boundary conditions on the fine mesh of the urban microscale flow model (one-way interaction), and furthermore permits feedback from the fine mesh to the coarse mesh (two-way interaction).

Some very preliminary work has been undertaken to couple urbanSTREAM (urban microscale flow model) with urbanGEM/LAM (urban mesoscale flow model). In this initial effort, only a one-way coupling between the two models has been attempted; namely, the flow predicted by urbanGEM/LAM over the region of interest was used to provide the boundary conditions required to specify the flow over a small sub-domain of this region where a high-resolution urban flow simulation was undertaken by urbanSTREAM. This down-scaling of flow information from urbanGEM/LAM to

urbanSTREAM was undertaken over a sub-domain of downtown Ottawa (see Fig. 18). In a future effort, the buildings surrounding this sub-domain (see Fig. 5) will be parameterized using the drag-force approach described in Section 3.

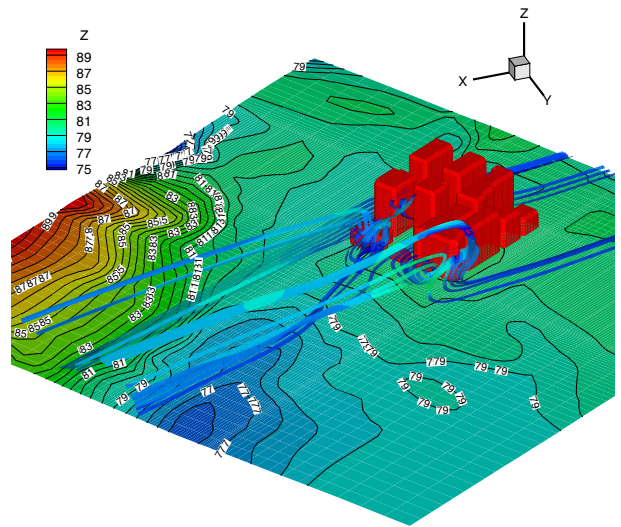


Figure 18: Flow over a block of buildings within the city of Ottawa.

6 CONCLUSIONS

Models for the prediction of the complex flow in the urban environment at the microscale have been developed, implemented, and validated against a number of comprehensive and detailed data sets obtained from wind tunnel and water channel simulations of flow over and through various building arrays. The models are based on a Reynolds-averaged Navier-Stokes (RANS) approach with the hierarchy of turbulence correlation closure models based on a phenomenological two-equation model for the turbulence kinetic energy (k) and viscous dissipation rate (ϵ).

Quantitatively, it was found that the prediction performance of these various steady-state RANS models was generally good – the quantitative agreement for the mean velocity is good, although the turbulence kinetic energy is generally underestimated by the models. An important conclusion of this study is that the standard k - ϵ turbulence-closure model with a linear eddy viscosity is perhaps the simplest complete turbulence

model that could be used for the prediction of urban flows on the microscale. This model may be useful as a general-purpose simulator of small-scale urban flows because it is robust and simple enough to be tractable numerically, and hence not require excessive computation time.

In the models described above, all the buildings in the cityscape were resolved explicitly in the sense that boundary conditions were imposed at all walls and roofs of every building. To reduce the computational cost of this approach, we investigated also the utility of representing groups of buildings in the cityscape in terms of a distributed drag force. To apply the distributed drag force model, we require the assignment of an appropriate value for the drag coefficient for a canopy consisting of an arbitrary geometrical arrangement of buildings. Although we were able to determine the drag coefficient for a regular array using high-resolution CFD results, empirical formulae proposed in the literature (e.g., [13]) will be employed when we conduct a real city simulation.

Finally, some effort was expended in interfacing the urban microscale flow model with urban databases. A capability for ingesting ShapeFiles (which stores non-topological geometry and attribute information for building/obstacle features in a data set) has been developed. This capability permits building data in a ShapeFile to be ingested directly into the urban microscale flow model, and an automatic scheme for generation of grids about the buildings imported within a specified flow domain has been designed and implemented. The grid information generated here can be imported directly into urbanSTREAM.

ACKNOWLEDGEMENTS

This work has been partially supported by Chemical Biological Radiological Nuclear Research and Technology Initiative (CRTI) program under project number CRTI-02-0093RD.

REFERENCES

- [1] K. Akselvoll and P. Moin, *Engineering Turbulence Modeling and Experiments*. **2**, 303 – 113 (1993).
- [2] M.J. Brown, R.E. Lawson, D.S. Decroix and R.L. Lee, *Report LA-UR-01-4138*, Los Alamos National Laboratory (2001).
- [3] C. Fureby and F. Grinstein, *J. Comput. Phys.* **181**, 68 – 97 (2002).
- [4] Y. Cheng, F.S. Lien, E. Yee and R. Sinclair, *Journal of Wind Engineering & Industrial Aerodynamics*. **91**, 1301 – 1328 (2003).
- [5] C. Beguier, I. Dekeyser and B. Launder, *Phys. Fluids*. **21**, 307 – 310 (1978).
- [6] A.M. Khokhlov, *J. Comput. Phys.* **143**, 519 – 543 (1998).
- [7] J. Larsson, F.S. Lien and E. Yee, ‘LES of High Reynolds Number Channel Flow on Coarse Grids’ *Proceedings of the 13th Annual Conference on CFD*, St. John’s, Newfoundland, Canada, 2005.
- [8] F.S. Lien and M.A. Leschziner, *Comput. Meth. Appl. Mech. Eng.* **114**, 123 – 148 (1994).
- [9] F.S. Lien and M.A. Leschziner, *Int. J. Num. Meth. Fluids*. **19**, 527 – 548 (1994).
- [10] F.S. Lien and E. Yee, *Boundary-Layer Meteorology*. **112**, 427 – 466 (2004).
- [11] F.S. Lien, E. Yee and J.D. Wilson, *Boundary-Layer Meteorology*. **114**, 245 – 285 (2005).
- [12] F.S. Lien and E. Yee, *Boundary-Layer Meteorology*. **114**, 287 – 313 (2005).
- [13] R.W. Macdonald, *Boundary-Layer Meteorology* **97**, 25 – 45 (2000).
- [14] E.R. Meinders and K. Hanjalic, *Int. J. Heat Fluid Flow* **20**, 255 – 267 (1999).
- [15] U. Piomelli and J. Liu, *Phys. Fluids A*. **7**, 839 – 848 (1995).
- [16] C. Rhie and W. Chow, *AIAA J.* **21**, 1525 – 1532 (1983).
- [17] T.H. Shih and N.S. Liu, *AIAA Paper: AIAA-2004-0160*, (2004).
- [18] M. Shur, P.R. Spalart, M. Strelet and A. Travin, *Engineering Turbulence Modeling and Experiments*. **4**, 669 – 678 (1999).
- [19] E. Yee and C. Biltoft, *Boundary-Layer Meteorology* **111**, 363 – 415 (2004).